PAPER

Check for updates

Investigation of energy storage performance in organic molecule-stabilized nickel ferrocyanide nanoparticles for supercapacitor applications†

Pooja Kumari,[a] Lungelo Lekokotla,[a] Chandan Saha,[a] Sarit K Ghosh, [iD][a] Harishchandra Singh[b] and Kaushik Mallick [iD] *[a]

Supercapacitors are gaining attention as an ideal energy storage solution due to their excellent specific power, fast charging rates and high durability. This study presents the development of an organic molecule stabilized nickel ferrocyanide (NFC) hybrid material, synthesized through a complexation-mediated approach, which demonstrates outstanding electrochemical performance, making it a promising candidate for high-efficiency supercapacitor applications. X-ray diffraction analysis confirms the formation of nickel ferrocyanide with a cubic crystal structure (space group: $Fm\bar{3}m$). Transmission electron microscopy analysis revealed spherical shaped nickel ferrocyanide particles within the size range of 2–4 nm. Fourier-transform infrared spectroscopy, Raman spectroscopy, and X-ray photo-electron spectroscopy confirmed the successful formation of nickel ferrocyanide and offered detailed insights into its bonding environment and chemical states. The electrochemical performance of the hybrid material displayed a specific capacitance of 298 F g^{-1} at 6 A g^{-1} and retained 88% of its original capacitance after 10 000 cycles in a three-electrode system. An asymmetric supercapacitor device, fabricated using NFC as the cathode and activated carbon as the anode electrode, delivered a specific capacitance of 94 F g^{-1} at 1.0 A g^{-1}. The device exhibited maximum specific energy and specific power values of 44 W h kg^{-1} and 6067 W kg^{-1}, respectively, with a moderately good cycle life (84% capacitance retention after 10 000 cycles). The results emphasize the potential of the NFC-based hybrid system as an efficient material for energy storage applications.

Introduction

The swift expansion of hybrid vehicles and electronic devices, coupled with the rising demand for clean and renewable energy, has driven significant efforts to investigate advanced energy storage technologies.[1,2] Attempts have been made by scientists and engineers to develop energy storage devices, such as solar cells, supercapacitors and batteries.[3–5] Supercapacitors have drawn significant interest in the field of electrochemical energy storage due to their distinctive advantages of fast charge and discharge speed, high specific power and long cycle life.[6]

Supercapacitor electrode materials are divided into different categories, such as carbonaceous materials, conductive polymer materials, and transition and post-transition metal-based

materials.[7–12] Among these electrode materials, transition-metal-based materials stand out as a crucial category, offering a balance between high capacitance, good electrical conductivity and stability, which are essential for the development of advanced supercapacitors.[13–15] However, the primary obstacles associated with transition metal-based electrode materials include their limited specific energy, high internal resistance and insufficient mechanical durability.[16,17] To address the aforementioned limitations, researchers have proposed several strategies for designing transition metal-based electrode materials. One such approach involves synthesizing nanostructured architectures that possess large specific surface areas and high porosity, which can influence electrochemical performance by improving ion diffusion, charge transfer, specific power, rate capability and overall stability.[18,19] In recent years, significant advancements have been reported in the performance of transition metal-based nanostructured oxides, sulfides and phosphides.[20–23] These materials have demonstrated noticeable improvements in energy storage ability, attributed to their unique structural properties, enhanced electrochemical stability and efficient charge transport mechanisms. Such progress highlights their potential for next-generation energy storage

[a] Department of Chemical Sciences, University of Johannesburg, P.O. Box. 524, Auckland Park, 2006, South Africa. E-mail: kaushikm@uj.ac.za

[b] Nano and Molecular Systems Research Unit, University of Oulu, FIN-90014, Finland

† Electronic supplementary information (ESI) available. See DOI: https://doi.org/10.1039/d5ma00352k

applications. Furthermore, various ternary and quaternary transition metal-based electrode materials have been extensively studied and shown to offer distinct advantages. These include a high density of redox-active sites, which facilitate efficient electrochemical reactions, as well as exceptional electrochemical stability, ensuring long-term performance and durability. These attributes make them highly promising candidates for advanced energy storage applications.[24,25]

Among the wide range of transition metal-based materials, nickel compounds have attracted significant attention and have been extensively investigated as promising pseudocapacitive electrode materials. This interest stems from their exceptionally high theoretical specific capacitance, remarkable thermal and chemical stability across various electrolyte systems, and ease of fabrication using cost-effective and scalable methods, which further enhance their suitability for next-generation energy storage applications.[26]

A nickel oxide, synthesized by a hydrothermal method, modified electrode demonstrated capacitances of 79 F g^{-1} in Na$_2$SO$_4$ and 132 F g^{-1} in KOH at 5 mV s^{-1} with excellent cycling stability in KOH electrolyte.[27] Nickel oxide and nickel hydroxide, synthesized through a chemical precipitation method, have displayed capacitance values of 171 F g^{-1} and 701 F g^{-1} at a specific current of 1 A g^{-1}, respectively. Notably, nickel hydroxide demonstrated excellent cycling stability, retaining 84.16% of its original capacitance after 5000 consecutive charge–discharge cycles in KOH (2.0 M) electrolyte.[28] The enhanced charge storage potential of hydroxide-based materials can be attributed to the improved mobility of electrolyte ions, which expedites efficient ion transport and redox reactions within the electrode structure.[28] The nickel sulfide–nickel sulfoselenide based supercapacitor exhibited high charge storage capability, achieving a high capacitance of 1908 F g^{-1} at a specific current of 1 A g^{-1}. The device retained 95% of its initial capacitance after 10 000 charge–discharge cycles at 25 A g^{-1}. Additionally, the device showed good shelf-life performance, retaining 100% capacitance after 3000 cycles at 10 A g^{-1}, after prolonged storage.[29] Nickel phosphide-based materials, characterized by their valence-rich nature, have received significant interest for energy storage applications. Honeycomb-like biphasic Ni$_5$P$_4$–Ni$_2$P exhibited a specific capacity of 1272 C g^{-1} at 2 A g^{-1}, demonstrating excellent rate capability. An asymmetric supercapacitor device, incorporating Ni$_5$P$_4$–Ni$_2$P as the positive electrode and activated carbon as the negative electrode, achieved high specific power and energy, highlighting its potential for supercapacitor applications.[30] The layered structure of a nickel-based metal–organic framework demonstrated high capacitance, remarkable cycling stability and excellent rate capability. It achieved a capacitance of 668 F g^{-1} at 10 A g^{-1} and 1127 F g^{-1} at 0.5 A g^{-1}, retaining 90% of its original capacitance after 3000 charge–discharge cycles.[31]

Layered double hydroxides, also known as hydrotalcite-like compounds, received significant research attention due to their promising electrochemical properties for energy storage and conversion applications.[32,33] A hybrid system of graphene nanosheet–Ni^{2+}/Al^{3+}-based layered double hydroxide, fabricated by a hydrothermal route, exhibited a maximum capacitance of 781.5 F g^{-1} with an excellent cycle life.[34] An asymmetric supercapacitor based on Ni–Co binary oxide demonstrated a maximum specific power of 3064 W kg^{-1} and specific energy of 10 W h kg^{-1}, highlighting its potential for energy storage applications.[35]

Research on hexacyanoferrate(II)-based materials remains limited, with only a handful of studies investigating their structural and electrochemical properties.[36] Despite their promising characteristics, including stability and distinctive electrochemical behavior, comprehensive research on the synthesis, performance, and optimization of these materials for energy storage and other technological applications remains limited. This gap in the literature underscores the need for further exploration of hexacyanoferrate(II)-based materials, particularly in the fields of supercapacitors, batteries, and other advanced material applications, to fully realize their potential in energy storage and related technologies. In this study, a complexation-mediated synthesis approach was developed to produce nickel ferrocyanide nanoparticles, which were subsequently utilized as the active material for constructing a hybrid supercapacitor. The synthesis process relied on the formation of a coordination complex, which enabled the controlled fabrication of nickel ferrocyanide nanoparticles with tailored properties, ensuring their suitability for high-performance energy storage applications.

Experimental

Materials

In this study, analytical-grade chemicals were used directly without further purification. Aniline, nickel chloride, potassium ferrocyanide, N-methyl pyrrolidine (NMP), potassium hydroxide (KOH), carbon black (CB), and polyvinylidene fluoride (PVDF) were obtained from Merck, while activated carbon (AC, Vulcan XC-72) was sourced from FUEL CELL Store.
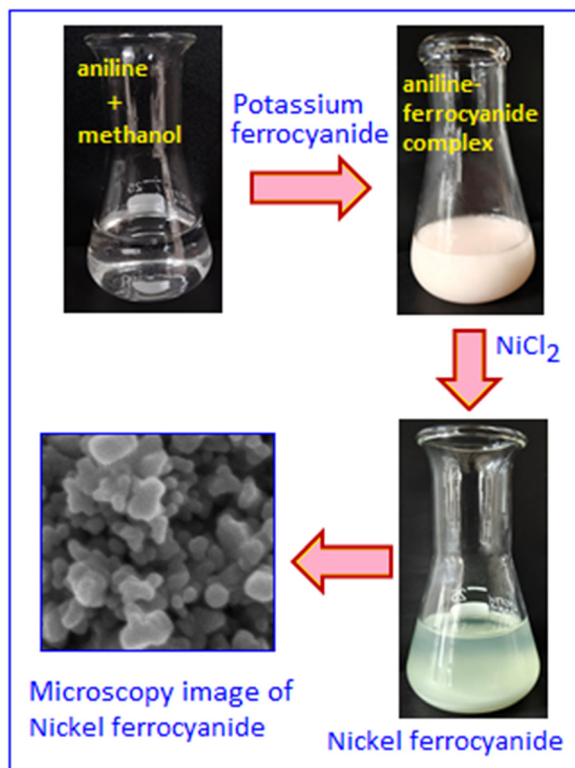
Synthesis of aniline stabilized nickel ferrocyanide (NFC) nanoparticles

To synthesize nickel ferrocyanide, 2 mL of aniline was dissolved in 10 mL of methanol and thoroughly mixed. In the next step, 5 mL of a 0.1 M aqueous potassium ferrocyanide solution was added dropwise to the methanolic aniline solution, yielding a white precipitate identified as a ferrocyanide–aniline complex. Subsequently, 4 mL of a 0.1 M nickel chloride solution was added to the above precipitate, resulting in a celadon green colour, which indicates the formation of nickel ferrocyanide (NFC; Scheme 1). The solid product was filtered, dried under vacuum and characterized using different analytical techniques. Furthermore, various electrochemical parameters of NFC were tested for energy storage applications.

Working electrode preparation for the three-electrode system

The working electrode material was prepared in the form of a slurry by combining NFC and PVDF (in a ratio of 9:1) in the presence of 20 μL of NMP as a solvent. The prepared slurry was coated onto a nickel foam substrate (1 × 1 cm^2) with a mass

Scheme 1 Schematic representation of the synthesis of organic molecule stabilized nickel ferrocyanide.

loading of 1.0 mg. After coating, the electrode was dried at 60 °C under vacuum.

Fabrication of the asymmetric supercapacitor

An asymmetric supercapacitor device was assembled using AC and NFC as the anode and cathode materials, respectively. The cathode electrode material of the device was prepared using NFC, CB and PVDF in a weight ratio of 8 : 1 : 1, while the anode electrode was fabricated using AC and PVDF in a 9 : 1 ratio, in NMP, in the form of a slurry. The prepared electrode materials

were deposited on two nickel foams and vacuum-dried at 60 °C. The electrodes were then separated using KOH-soaked filter paper and assembled into a CR2032-type coin cell.

Materials characterization

The instrumental methods used for characterization of the synthesized material are described in our previous publications,[11,37] including X-ray diffraction (XRD, Philips PANalytical X'pert diffractometer), transmission electron microscopy (TEM, JEOL JEM-2100), Fourier transform infrared spectroscopy (FTIR, Shimadzu IRSpirit-X), scanning electron microscopy (SEM, JEOL JSM-840), Raman spectroscopy (Jobin-Yvon T64000), and X-ray photoelectron spectroscopy (XPS, Thermo Scientific MultiLab 2000). All the electrochemical experiments were conducted using a Bio-Logic SP300. Both the cyclic voltammetry (CV) and galvanostatic charge–discharge (GCD) experiments were performed in 1.0 M KOH aqueous solution. Electrochemical impedance spectra (EIS) were recorded within the frequency range of 10 mHz to 100 kHz at 10 mV using a Bio-Logic SP200. The equations used to extract the electrochemical parameters are available in the ESI.†

Results and discussion

The reaction between aniline and potassium ferrocyanide resulted in precipitation due to the formation of a ferrocyanide–aniline complex, which arises from the coordination between the amino group of aniline and ferrocyanide ions. This complex subsequently reacted with nickel chloride to form nickel ferrocyanide, with aniline molecules acting as a support matrix. The crystal structure of the nickel ferrocyanide sample was characterized by XRD measurements. Fig. 1A shows the characteristic diffraction peaks of the material, indexed with ICDD reference number 00-057-0049. The sharp diffraction peaks indicate high crystallinity of the material with lattice parameter values of $a = b = c = 10.05$ Å and $\alpha = \beta = \gamma = 90°$. Nickel ferrocyanide forms a symmetric cubic structure with a space group of $Fm\bar{3}m$ (225). The XRD pattern shows peaks at 17.24°, 24.54°, 29.34°, 35.39°, 39.56°,
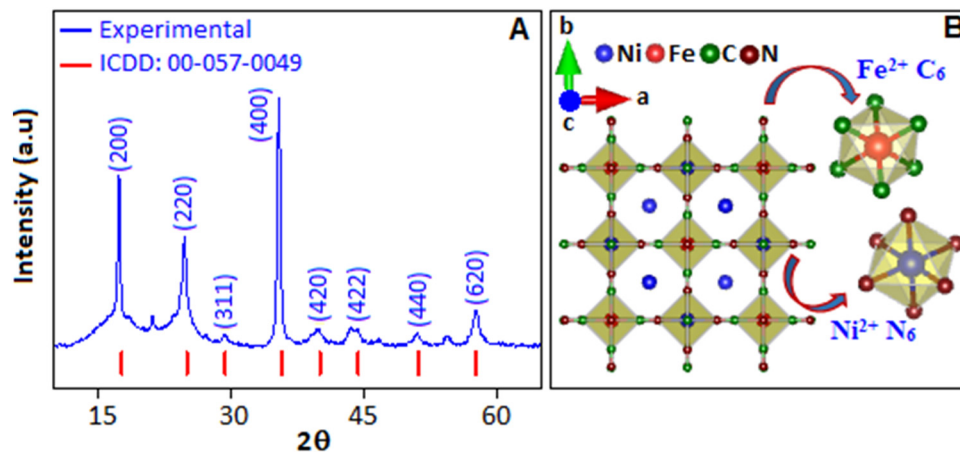

Fig. 1 (A) XRD pattern and (B) unit cell representation of nickel ferrocyanide.

43.77°, 51.29° and 57.75°, which correspond to (200), (220), (311), (400), (420), (422), (440) and (620) crystallographic planes. The crystal structure of the synthesized material is shown Fig. 1B, which reveals a distorted framework composed of Fe(II)–C≡N–Ni(II) skeletons, with alternating $Fe^{2+} C_6$ and $Ni^{2+} N_6$ octahedra along the three Cartesian directions, connected by cyanide bridges.[36,38]

Fig. 2A shows the scanning electron microscopy image that reflects the surface morphology of the hybrid system. The material is a combination of organic and inorganic components, with the aniline contributing to the organic part that stabilizes the nickel ferrocyanide. The elemental mapping shows uniform distributions of Ni, Fe, C and N in nickel ferrocyanide (Fig. 2(B–E)). The color-coded maps, generated by the energy dispersive X-ray detector, illustrate the distribution of various elements in the sample and correspond to a specific element. The mapping further confirms that aniline and nickel ferrocyanide are thoroughly integrated at the microscopic level, showing no significant segregation of the components. The energy-dispersive X-ray spectrum in Fig. 2F further confirms the presence of Ni, Fe, C, and N in the sample, with distinct peaks corresponding to each element. These peaks represent characteristic X-ray emissions, verifying the elemental composition.

Furthermore, transmission electron microscopy was used to examine the size and shape of the nickel ferrocyanide particles within the organic matrix. Fig. 3(A and B) presents microscopy images of aniline-stabilized nickel ferrocyanide with different magnifications. The dark spots visible in the image (Fig. 3B) represent the individual nickel ferrocyanide nanoparticles within the size range of 2–4 nm, uniformly dispersed throughout
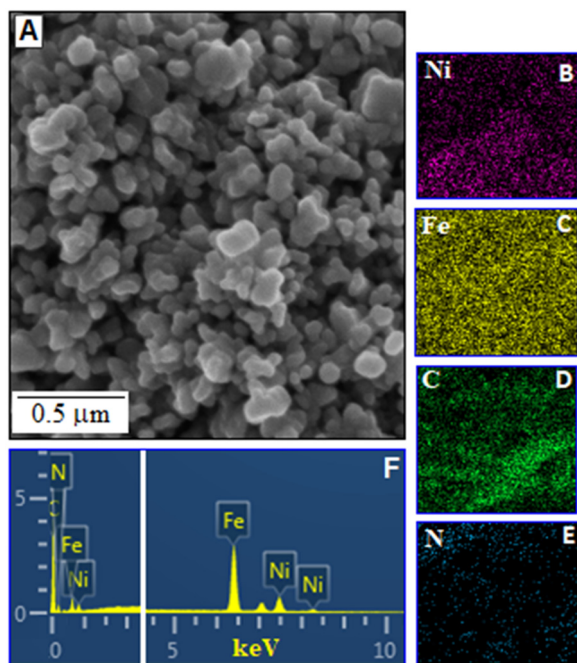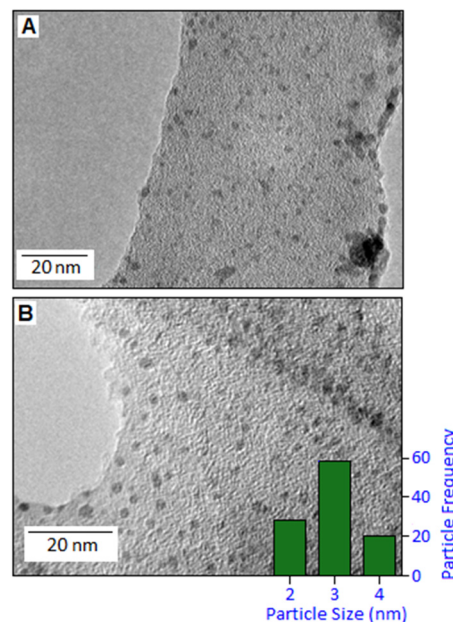

Fig. 3 TEM images (A) and (B) of nickel ferrocyanide nanoparticles with different magnifications. The inset in figure (B) shows the histogram.

the organic matrix. The inset histogram shows the size distribution of the nickel ferrocyanide particles.

Fig. 4A displays the FTIR spectrum of NFC nanoparticles, with sharp peaks at 2023.9, 2025.6 and 2047.4 cm^{-1} corresponding to the –C≡N stretching vibration. These peaks are shifted from the typical cyano-group peak at 2600 cm^{-1}, indicating the coordination of the cyano group with nickel, which donates electrons to the metal ion.[39,40] The peak at 586.4 cm^{-1} represents the deformation vibration of –Fe(II)–C≡N, while the peak at 448.9 cm^{-1} corresponds to the deformation vibration of –C≡N–Ni(II).[41] The Raman spectra reveal two distinct peaks at 2103 and 2139 cm^{-1}, which are indicative of cyanide stretching (Fig. 4B). The peaks at 245 and 352 cm^{-1} correspond to Ni–N stretching, while the peak at 517 cm^{-1} is linked to Fe–C stretching vibrations.[42,43]

X-ray photoelectron spectroscopy was used to further analyse the chemical compositions of NFC. The survey spectrum in Fig. 5A indicates the presence of Ni, Fe, N and C elements in the NFC. The Ni $2p_{3/2}$ and Ni $2p_{1/2}$ peaks observed at 856.36 and 874.0 eV, respectively, with the satellite peaks appearing at 862.6 and 880.8 eV, correspond to Ni^{2+} (Fig. 5B).[44] The high-resolution Fe 2p spectrum shows two peaks at 708.5 and 721.3 eV along with the satellite peaks at 715 and 735 eV, which correspond to Fe $2p_{3/2}$ and Fe $2p_{1/2}$, respectively, indicating the presence of Fe^{2+} in the sample (Fig. 5C).[45] The major peaks for the C 1s and N 1s spectra (Fig. 5D and E) were deconvoluted into two components at 398.4 and 285.3 eV, indicating the presence of C–N in NFC.[45] The synthesized compounds exhibit minor peaks at 286.8 and 400.2 eV, which imply the presence of defective C≡N sites in the Fe–CN–Ni bridging.[46]

Electrochemical analysis (three-electrode system)

The electrochemical behaviour of the NFC-modified working electrode was assessed using the cyclic voltammetry technique
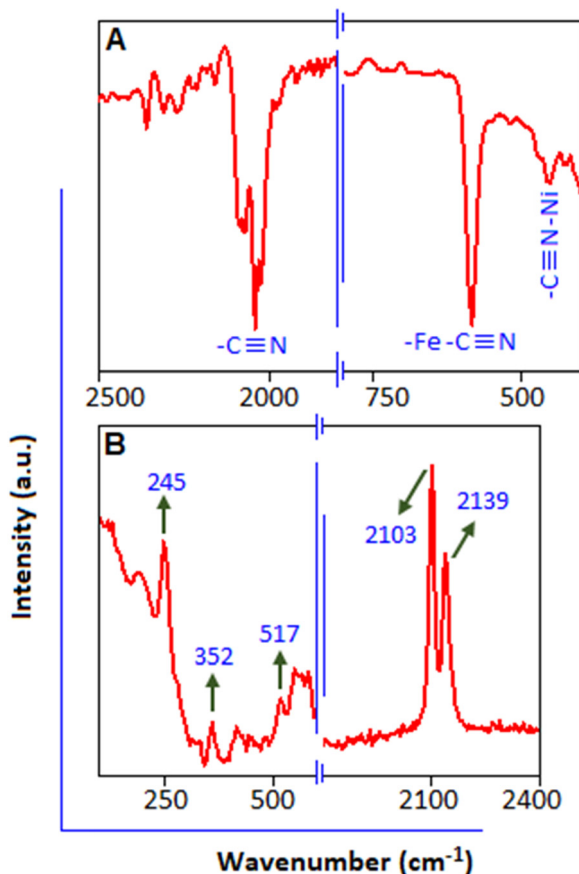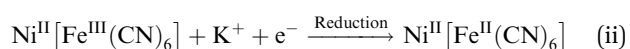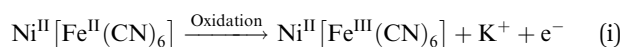

Fig. 2 (A) SEM image of an aniline−nickel ferrocyanide hybrid system. The elemental mapping of nickel(II) ferrocyanide: (B) nickel, (C) iron, (D) carbon and (E) nitrogen. (F) Energy dispersive X-ray spectrum.

Fig. 4 (A) Fourier transform infrared spectrum and (B) Raman spectrum of nickel ferrocyanide.

Fig. 5 (A) XPS survey spectrum of nickel ferrocyanide. High resolution deconvoluted XPS spectrum of (B) Ni 2p, (C) Fe 2p, (D) C 1s and (E) N 1s.

with a standard three-electrode setup, which included a saturated calomel electrode as the reference electrode and a platinum wire as the counter electrode in the presence of 1.0 M KOH electrolyte solution, within a potential window of 0.0 to 0.6 V. The CV curves recorded at scan rates ranging from 5 to 100 mV s^{-1} exhibit faradaic behavior with excellent redox characteristics (Fig. 6A). The voltammogram at 5 mV s^{-1} shows a prominent oxidation peak at 0.5 V and the corresponding reduction peak at 0.37 V (Fig. 6A, inset). Ni(II) does not show any characteristic pattern in the CV profile within the potential range of 0–1.0 V, and the faradaic current is only attributed to electron transfer between the Fe^{II}/Fe^{III} redox couple, which shows electrochemical reversibility.[47,48] To maintain charge neutrality, charge transfer between the Fe^{II}/Fe^{III} redox couple occurred due to the intercalation and deintercalation of K$^+$ ions, from the electrolyte, in the NFC system.[36,49]

$$Ni^{II}\left[Fe^{II}(CN)_6\right] \xrightarrow{\text{Oxidation}} Ni^{II}\left[Fe^{III}(CN)_6\right] + K^+ + e^- \quad \text{(i)}$$

$$Ni^{II}\left[Fe^{III}(CN)_6\right] + K^+ + e^- \xrightarrow{\text{Reduction}} Ni^{II}\left[Fe^{II}(CN)_6\right] \quad \text{(ii)}$$

With increasing scan rate, both anodic and cathodic peak currents showed an upward trend, leading to a higher integrated area in the voltammograms, which signifies the good
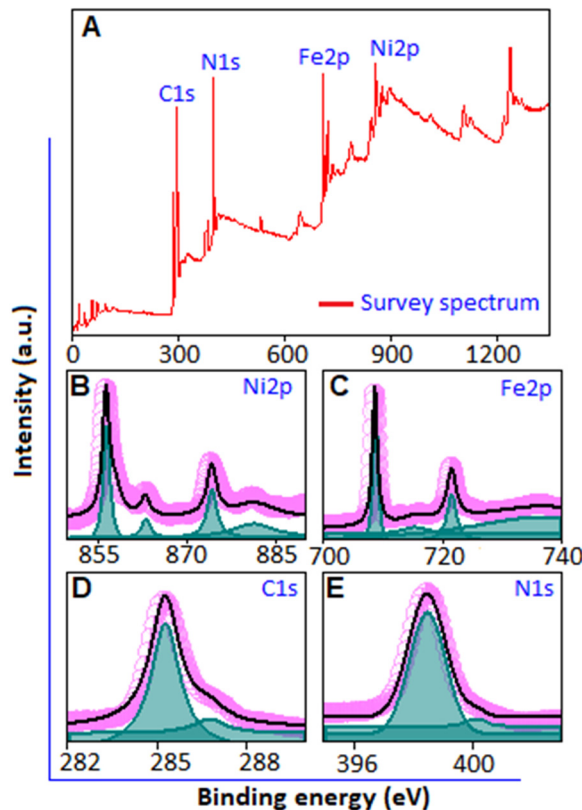
rate capability, with 41% capacitance retention, of the NFC based electrode.

To assess the energy storage performance of the NFC-modified electrode, the GCD test was performed. Fig. 6B displays the GCD curves at specific currents ranging from 20 to 6 A g^{-1} and the pattern of the charging curves are nearly symmetrical with the discharging curves. A plateau-like feature was observed in both charge–discharge curves, highlighting the intercalation and deintercalation of K$^+$ into the active material.[50] The maximum specific capacitance of 298 F g^{-1} was achieved at 6 A g^{-1}, which decreased to 39 F g^{-1} at 20 A g^{-1}, calculated using eqn (S1) (ESI†). The specific capacitance gradually decreased with increasing specific current (Fig. 6C). This drop is due to the limited accessibility of electrolyte ions into the electrode material.

To assess the stability of the NFC-based electrode material, 10 000 repetitive charge–discharge cycles were performed at a current density of 6 A g^{-1} (Fig. 6D). After completion of the cycles, 88% of the specific capacitance and 95% of the coulombic efficiency were retained. The 1st and 10 000th GCD profiles are displayed in the inset of Fig. 6D. To enhance long-term cycling stability, various strategies can be implemented during the electrode fabrication process, such as optimizing the structure and surface of the active material, incorporating conductive additives like carbon-based materials, and utilizing flexible, robust binders to preserve electrode integrity.
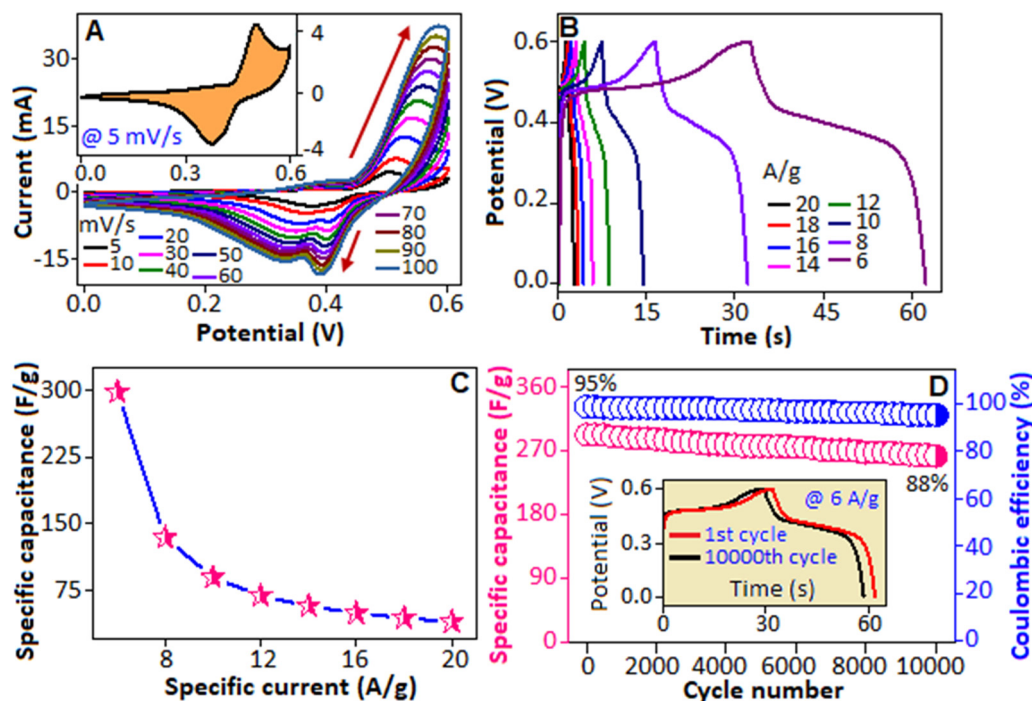
Fig. 6 (A) Cyclic voltammogram of the NFC-modified electrode at scan rates ranging from 5 to 100 mV s^{-1}. The inset shows the voltammogram at 5 mV s^{-1} with an oxidation peak at 0.5 V and a reduction peak at 0.37 V, which corresponds to electron transfer between the Fe^{II}/Fe^{III} redox couple. (B) Galvanostatic charge–discharge profile of the NFC-modified electrode under various current densities ranging from 20.0 to 6.0 A g^{-1}. (C) Graphical representation of specific capacitance as a function of specific current. (D) Capacitance retention and coulombic efficiency of the NFC-based electrode for 10 000 cycles at 6.0 A g^{-1}. The inset shows the GCD profile for the 1st and 10 000th cycles.

To evaluate the structural stability of the NFC-based electrode, XRD and Raman spectroscopy were performed before and after 10 000 charge–discharge cycles, as shown in Fig. S1A and B (ESI†), respectively. The XRD pattern of the as-prepared NFC electrode (shown in red colour) exhibits sharp diffraction peaks corresponding to the crystalline phases of nickel ferrocyanide, confirming a well-ordered structure. After cycling, a noticeable decrease in peak intensity is observed in the XRD pattern (shown in blue colour), suggesting slight structural degradation of the electrode material due to prolonged potential stress. The XRD pattern of the Ni foam substrate, shown in green, is included as a reference. Raman spectroscopy analysis of the used NFC electrode was carried out to further examine the structural stability of the active material. Fig. S1B (ESI†) shows the comparative Raman spectra, recorded before and after 10 000 cycles, which reveal a slight quenching in peak intensities signifying minor structural degradation of the material. Despite the observed spectral changes, the key structural features of the electrode material remain detectable, confirming that the material retains its crystallinity and integrity. This nominal degradation corresponds to the minor drop in coulombic efficiency and capacitance retention, observed during electrochemical testing, further validating the long-term stability of the material for supercapacitor applications.

Charge storage mechanism

The charge storage mechanism of the electrode includes two parameters such as the capacitance of the electric double layer and the diffusion-controlled redox reaction of the electrochemically active material.[51] The power law relationship was utilized to evaluate the charge storage behaviour of the NFC-modified electrode:

$$I_p = av^b \tag{iii}$$

$$\log(I_p) = b\log(v) + C \tag{iv}$$

where I_p denotes the peak current, a and b are constants and v is the scan rate. The slope of the straight line equation determines the 'b' value, which is 0.5 for a diffusion-controlled (D_C) process and 1.0 for a capacitive-controlled process (C_C). For the NFC-modified electrode, the b values of 0.57 (for the anodic peak) and 0.53 (for the cathodic peak) were obtained (Fig. 7A), indicating that the diffusion-controlled process is the predominant mechanism for the charge storage.

By analysing the CV behaviour at varying scan rates, the contributions from D_C and C_C charge storage can be differentiated. The NFC-modified electrode exhibits both reversible redox reactions (faradaic) and ionic adsorption/desorption (non-faradaic) phenomena. The peak current (I_p) is attributed to both D_C and C_C:

$$I_p = C_C + D_C \tag{v}$$

$$C_C = k_1 v \tag{vi}$$

$$D_C = k_2 v^{1/2} \tag{vii}$$
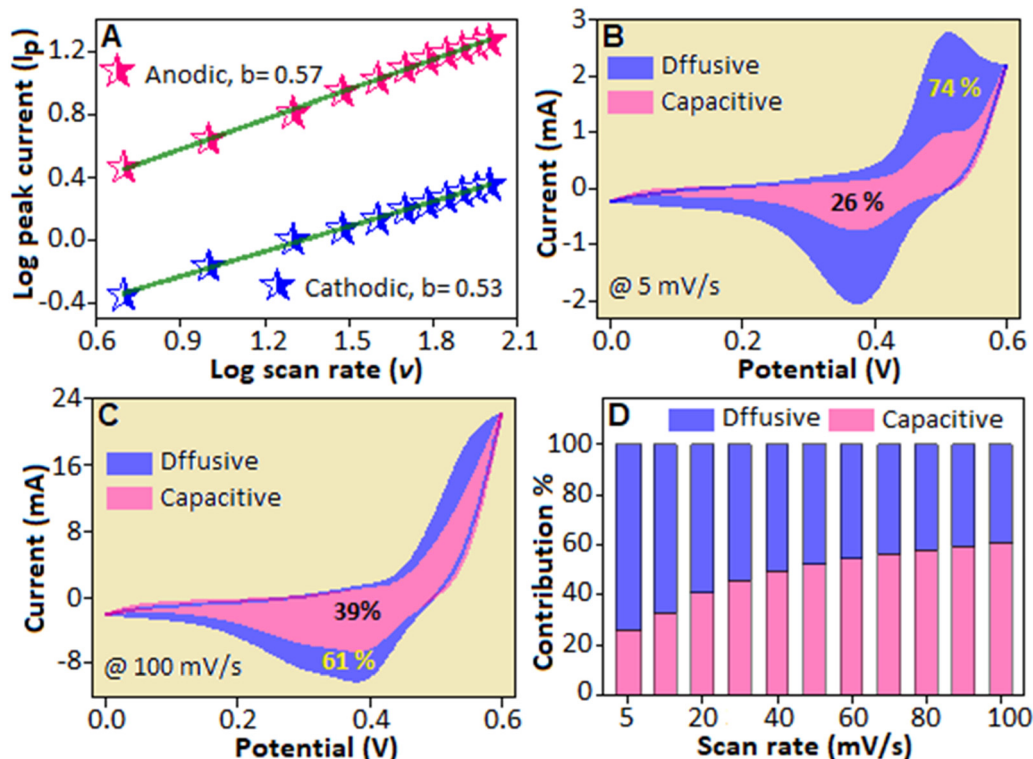
$$I_p = k_1 v = k_2 v^{1/2} \tag{viii}$$

Fig. 7 (A) Graphical representation of peak current (I_p) as a function of the scan rate (v) in a log scale. (B) and (C) Voltametric representation of the diffusive and capacitive contributions of the electrode material at 5 and 100 mV s⁻¹, respectively. (D) Diffusive and capacitive charge storage contributions (%) of the electrode material under various scan rates (5–100 mV s⁻¹), represented by a bar graph.

[by substituting the values of C_C and D_C in eqn (viii)]

$$I_p/v^{1/2} = k_1 v^{1/2} + k_2 \qquad \text{(ix)}$$

k_1 (slope) and k_2 (intercept) can be extracted by plotting $I_p/v^{1/2}$ versus $v^{1/2}$ (Fig. S2, ESI†). Fig. 7B and C illustrates the CV curves at a scan rate of 5 and 100 mV s⁻¹. The blue shaded area represents the diffusive-controlled contribution, while the pink shaded area of the curve represents the capacitive-controlled contribution. Fig. 7D presents a bar graph showing the contribution (%) of capacitive- and diffusive-controlled processes in overall performance at different scan rates. The electrode exhibits a diffusive contribution of 39% at 100 mV s⁻¹, which is enhanced to 74% at 5 mV s⁻¹. It was observed that the diffusive contribution increases as the scan rate decreases. At lower scan rates, the charges have more time to interact with the electrode material, allowing the diffusion process to become more significant. This increased interaction time allows more ions or charge carriers to diffuse to and from the electrode surface, enhancing the diffusive contribution to the electrochemical behavior.

Impedance property of the three-electrode system

Electrochemical impedance spectroscopy (EIS) studies were carried out using a NFC-modified electrode to study the impedance characteristics associated with ion diffusion at the electrode–electrolyte interface within the frequency range from 10 mHz to 100 kHz at 10 mV. Fig. 8A displays the Nyquist plot

of the spectrum, with a magnified view of the high-frequency region shown in inset (I). The equivalent circuit model of the Nyquist plot is illustrated in inset (II) of Fig. 8A. The model includes the solution resistance (R_S), which accounts for the resistance of the electrolyte. The constant phase elements Q_2 and Q_3 are introduced into the circuit, which indicates the non-ideal capacitive behaviour of the system, also reflecting the surface roughness or heterogeneity of the electrode. The charge transfer resistance (R_{CT}) represents the resistance to the movement of charge species during the electrochemical reaction. Warburg impedance (Z_W) describes the diffusion-controlled behaviour of electrolyte ions, representing the resistance to ion movement at the interface between the electrode and electrolyte.[52,53] The Nyquist plot consists of a semi-circular pattern in the high-frequency region, which signifies the controlled process of charge transfer, followed by an inclined linear segment in the low-frequency region, reflecting the dominance of electrolyte ion diffusion in the energy storage mechanism. The extracted R_S and R_{CT} values are 0.6 and 3.2 Ω, respectively. The electrochemical behavior of the NFC-modified electrode in the presence of KOH electrolyte is described as follows. The faradaic reaction, as indicated by CV and GCD profiles, was governed by the diffusion of OH⁻ ions onto the electrode surface. The linear pattern of the Nyquist plot in the low-frequency region further supports the dominance of electrolyte ion diffusion.[53] The mathematical expression for faradaic impedance (Z_F) is expressed as the sum of the charge transfer
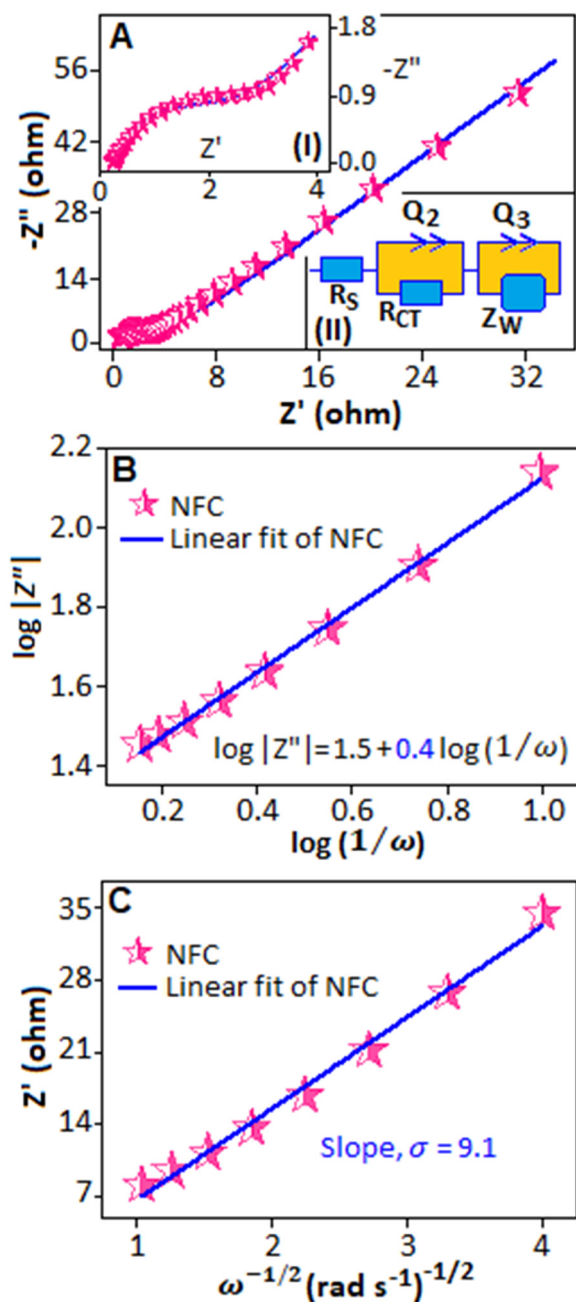
Fig. 8 (A) Nyquist plot of the NFC-modified electrode. Inset (I): magnified image of the Nyquist plot for the high-frequency region; inset (II): the equivalent circuit model. (B) Graphical representation of $\log|Z''|$ vs. $\log(1/\omega)$. (C) Graphical representation of Z' (Ohm) vs. $\omega^{-1/2}$ (rad s^{-1})$^{-1/2}$.

resistance and the impedance associated with the diffusion-controlled process, $Z_F(\omega) = R_{CT} + Z_W(\omega)$, where ω represents the angular frequency. For $\omega \rightarrow \infty$, the electrochemical performance is influenced by charge transfer processes, while $\omega \rightarrow 0$ represents the diffusion-controlled electrochemical behaviour.[54] The impedance (Z_W) at an angular frequency (ω) can be expressed as: $Z_W(\omega) = \sigma/\omega^\alpha(1-j)$ or $\log|Z''| = \log \sigma + \alpha \log(1/\omega)$, where σ, j and α represent the Warburg coefficient, imaginary unit and transfer coefficient.[55] The transfer coefficient (α) is derived from the slope

of the linear plot, $\log|Z''|$ versus $\log(1/\omega)$ (Fig. 8B), which illustrates the electrochemical performance of the electrode materials (α corresponds to 0.5 for Warburg behaviour). The slope of the straight line yields the transfer coefficient value of 0.4, signifying Warburg behaviour of the electrode material. The above information serves as additional confirmation of the diffusion-controlled process as suggested by the CV analysis. Furthermore, the diffusion coefficient (D) for OH$^-$ ions is calculated from the following equation:

$$D = R^2T^2/2A^2n^4F^4C^2\sigma^2 \qquad (x)$$

where R refers to the gas constant, T is the temperature, A is the surface area, n is the number of electrons transferred, F denotes the Faraday constant, C is the molar concentration of OH$^-$ ions and σ is the Warburg coefficient, extracted from the slope of the Z' versus $\omega^{-1/2}$ linear plot (Fig. 8C).[54] The estimated diffusion coefficient was obtained as 3.9×10^{-6} cm^2 s^{-1}. The results of impedance analysis illustrate a small charge transfer resistance and an enhanced diffusion coefficient, facilitating a rapid electrochemical reaction with excellent supercapacitor performance. Based on the above electrochemical results, the NFC-modified electrode was used as a cathode to assemble an asymmetric device.

Electrochemical analysis of the asymmetric device

In order to explore the practical application of the synthesized material, an asymmetric supercapacitor was built with AC serving as the negative electrode and NFC as the positive electrode. The mass ratio of the AC and NFC was calculated according to mass balance theory. The mass ratio was obtained as 2.0, calculated using the specific capacitance of AC- and NFC-modified electrodes at a specific current of 6 A g^{-1} (eqn (S2), ESI†). The total mass of active material used for the device was 3 mg. Fig. 9A shows the comparative CV curves of AC (-0.7 to 0.0 V) and NFC (0.0 to 0.6 V) modified electrodes at a scan rate of 5 mV s^{-1} in a three-electrode cell. The combined voltage window for the device was 1.3 V. Fig. 9B displays the CV curves for the device, recorded at scan rates ranging from 5 to 100 mV s^{-1}. The voltammograms demonstrate a faradaic charge storage mechanism (Nernstian process).[54] The electrochemical performance of the device was further evaluated using the GCD analysis. Fig. 9C illustrates the GCD profile of the device at various specific currents between 4.3 and 1.0 A g^{-1}. The non-linear charge–discharge pattern clearly demonstrated that the charge storage process was performed through a redox reaction and the estimated specific capacitance values were 18 and 94 F g^{-1} at specific currents of 4.3 and 1.0 A g^{-1}, respectively (eqn (S1), ESI†). It is evident from Fig. 10A that the specific capacitance values decreased gradually with increasing specific current, which was due to inadequate penetration of electrolyte ions into the electrode material. The stability of the device was evaluated through 10 000 repetitive GCD cycles at a specific current of 3.0 A g^{-1}. The calculated Coulombic efficiency and capacity retention values were 96% and 84%, respectively, as displayed in the upper panel of Fig. 10B. We further studied the charge storage mechanism of the device
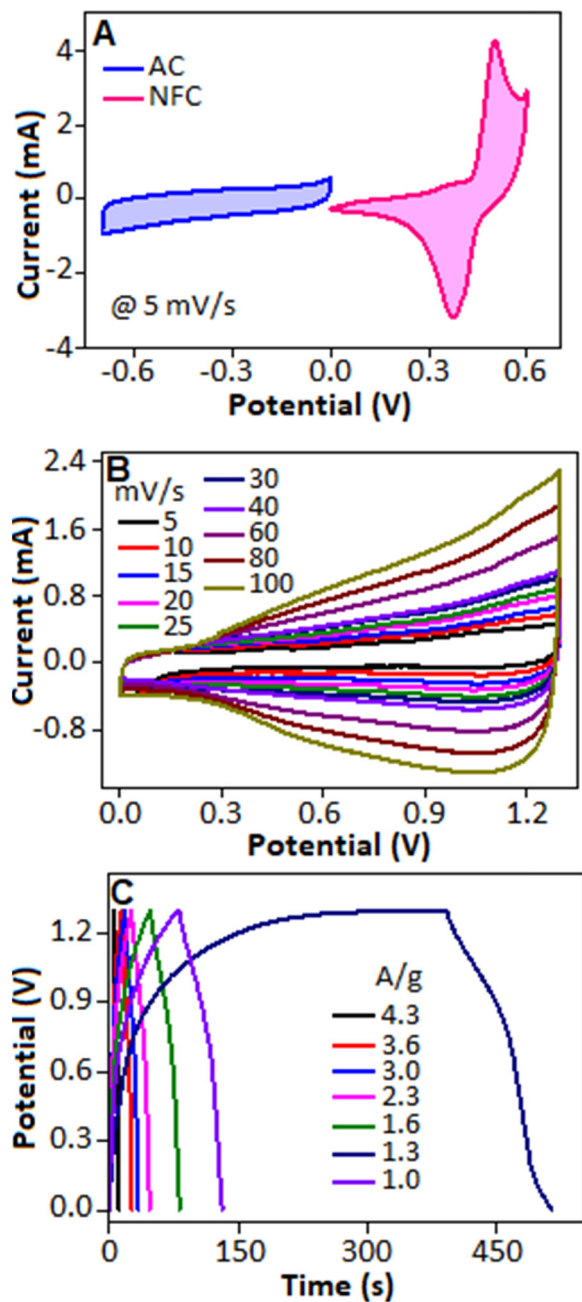
Fig. 9 (A) Comparative CV profiles of AC- and NFC-modified electrodes at 5 mV s⁻¹. (B) Voltammograms of the hybrid device under various scan rates in the range of 5–100 mV s⁻¹. (C) Galvanostatic charge–discharge profile of the device under various current densities ranging from 4.3 to 1.0 A g⁻¹.
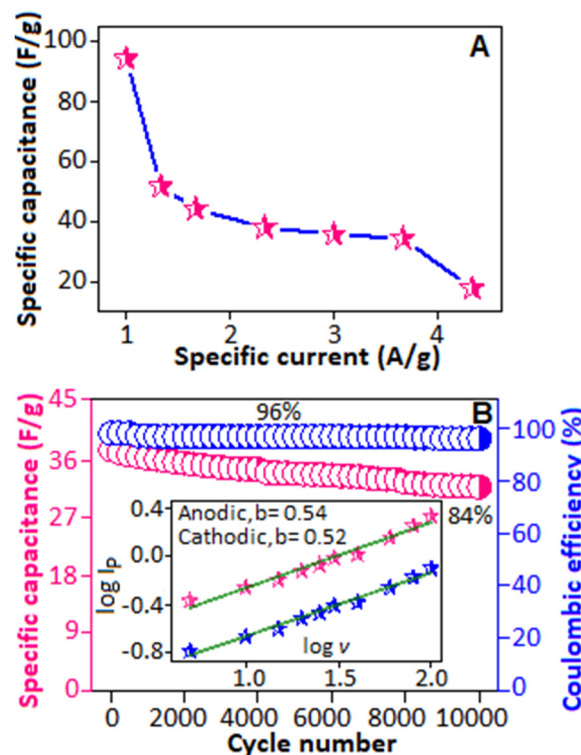

Fig. 10 (A) Graphical representation of specific capacitance as a function of specific current. (B) Specific capacitance and coulombic efficiency of the device at 3.0 A g⁻¹ for 10 000 GCD cycles (upper panel). Linear fitting of the anodic and cathodic peak currents (lower panel).

6067 W kg⁻¹, respectively. The electrochemical parameters of some ferrocyanide based materials, used for supercapacitor applications, are presented in Table 1.[36,56–59]

Impedance properties of the device

Fig. 11B presents the Nyquist plot before and after GCD cycles (main panel) and the corresponding equivalent circuit of the device (inset). In the Nyquist plot, a slight change in the slope in the lower frequency region was observed before and after GCD cycles. This change could be attributed to repeated cycling, voltage drop, polarization, and the reduction of active sites caused by high current density.[60] The solution resistance (R_S) and charge transfer resistance (R_{CT}) values were initially 1.3 Ω and 62 Ω, respectively, before cycling and decreased to 0.77 Ω and 57.7 Ω after 5000 GCD cycles, suggesting degradation of the electrode material. The Bode plot (phase angle *vs.* frequency), shown in Fig. 11C, presents a phase angle value of $-80°$ in the low-frequency region, which is indicative of a near-capacitive behaviour of the device.[61] Fig. 11D shows the variation of real and imaginary capacitance, $C'(\omega)$ and $C''(\omega)$, with frequency. The $C'(\omega)$ and $C''(\omega)$ values are calculated using the equations: $Z'(\omega) = 2\pi f C''(\omega)|Z(\omega)|$ and $Z''(\omega) = 2\pi f C'(\omega)|Z(\omega)|$,[61,62] where ω is the angular frequency, $\omega = 2\pi f$, f is frequency and Z represents the impedance. The accessible and transferrable real capacitance value of the device was obtained as 0.73 mF at 0.1 Hz. The imaginary capacitance, with

using the power law equation (eqn (S2), ESI†), as mentioned above. The obtained anodic and cathodic *b*-values are 0.54 and 0.52, respectively, indicating a dominant diffusion-controlled process (Fig. 10B, lower panel). The Ragone plot in Fig. 11A describes the relationship between the specific power and specific energy as a function of specific current, calculated using eqn (S3) and (S4) (ESI†). The maximum specific energy and specific power values were obtained as 44 W h kg⁻¹ and
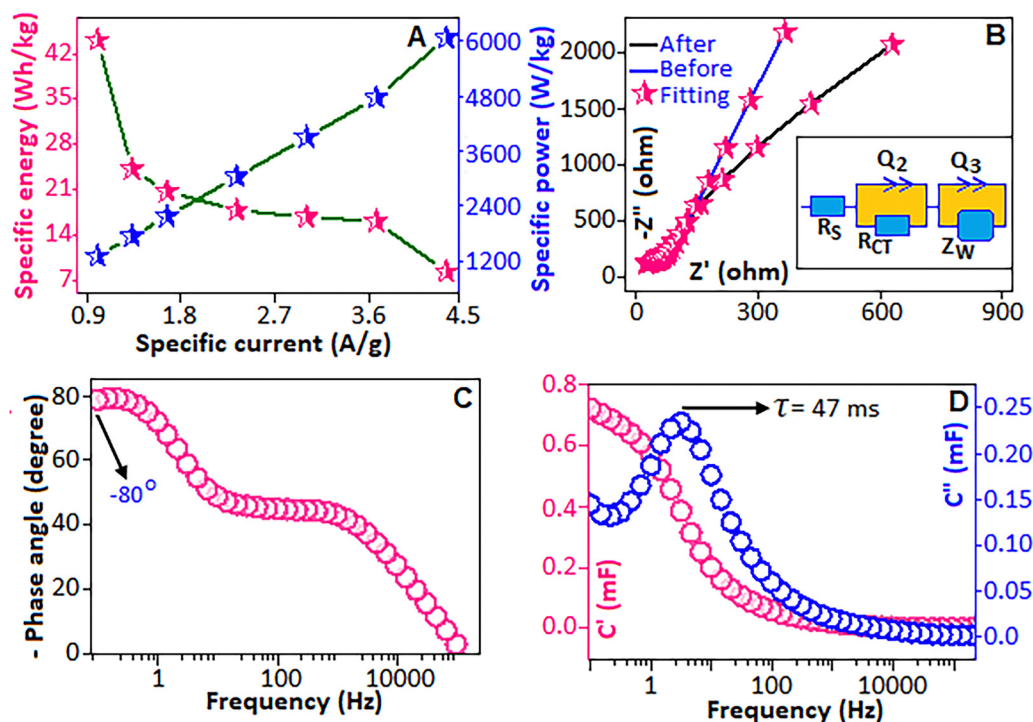
Fig. 11 (A) Graphical representation of specific power and specific energy as a function of specific current. (B) Nyquist plot of the device before and after GCD cycling. Inset: Equivalent circuit model. (C) Graphical representation of phase angle as a function of frequency and (D) real capacitance (C') and imaginary capacitance as a function of frequency.

Table 1 Comparison of the supercapacitive performance of hexacyanoferrate based materials

Entry	Material	Electrolyte	Specific capacitance/capacity	Specific energy	Specific power	Ref.
1	NiHCF	0.5 M Na_2SO_4	7.3 mF cm^{-2}@0.1 mA cm^{-2}	0.65 mW h cm^{-2}	0.4 mW cm^{-2}	36
2	Ni–HCF	1.0 M Na_2SO_4	6.9 C cm^{-2}@0.1 A cm^{-2}	36 W h kg^{-1}	200 W kg^{-1}	56
3	Co–rGOH	1.0 M KNO_3	102 F g^{-1}@1 A g^{-1}	57.5 W h kg^{-1}	10 kW kg^{-1}	57
4	CoHCF	PVA/KOH	47 F g^{-1}@2 A g^{-1}	5.3 W h kg^{-1}	1800 W kg^{-1}	58
5	CoHCF–MnO_2	0.5 M Na_2SO_4	76.3 F g^{-1}@0.5 A g^{-1}	37.6 W h kg^{-1}	1.1 kW kg^{-1}	59
6	NFC	1.0 M KOH	94.0 F g^{-1}@1 A g^{-1}	44 W h kg^{-1}	6067 W kg^{-1}	This work

Ni–HCF: nickel hexacyanoferrate; Co–rGOH: cobalt hexacyanoferrate–reduced graphene oxide hydrogels; CoHCF: cobalt hexacyanoferrate

Table 2 Comparative electrochemical parameters of NFC-based three-electrode and two-electrode systems

Entry	Three-electrode system	Two-electrode system
Electrolyte	1.0 M KOH	1.0 M KOH
Mass loading	1.0 mg	3.0 mg
Specific capacitance	298 F g^{-1}@6.0 A g^{-1}	94 F g^{-1}@1.0 A g^{-1}
Capacitance retention	88%@10 000 cycles	84%@10 000 cycles
Coulombic efficiency	96%@10 000 cycles	95%@10 000 cycles
Solution resistance	0.6 Ω	3.2 Ω
Charge transfer resistance	0.77 Ω	57.7 Ω

a peak maximum value of 0.72 mF at 3.36 Hz corresponding to a relaxation time τ of 47 ms, demonstrated the full charging time of the device. The electrochemical parameters for both NFC-based three-electrode and two-electrode systems are summarized in Table 2, as a ready reference.

Conclusion

Nickel ferrocyanide was successfully synthesized *via* a complexation-mediated route, enabling the controlled formation of inorganic nanoparticles with a narrow size distribution, stabilized by an organic matrix. The electrochemical performance of a nickel ferrocyanide-modified electrode in a three-electrode system demonstrated significant faradaic behavior linked to the Fe^{II}/Fe^{III} redox couple, achieving a specific capacitance of 298 F g^{-1} at 6 A g^{-1} with excellent cycling stability. An asymmetric supercapacitor, utilizing the title material as the cathode, operated within a 1.3 V potential window and exhibited a specific capacitance of 94 F g^{-1} at 1.0 A g^{-1} with the maximum specific energy and specific power values of 44 W h kg^{-1} and 6067 W kg^{-1}, respectively. The device demonstrated excellent durability, retaining 84% of its initial capacitance after 10 000 galvanostatic charge–discharge cycles, which indicates

the strong structural stability and electrochemical robustness of the material, making it a promising candidate for energy storage applications.

Data availability

Data will be made available upon request.

Conflicts of interest

The authors declare no competing financial interests.

Acknowledgements

References

1 S. Fiorenti, J. Guanetti, Y. Guezennec and S. Onori, *J. Power Sources*, 2013, **241**, 112–120.

2 L. Samyn, T. Lessa, R. S. Babu, A. Kalaivani, T. Barbosa and A. de Barros, *Mater. Adv.*, 2023, **4**, 3654–3661.

3 P. Nayak, S. Mahesh, H. Snaith and D. Cahen, *Nat. Rev. Mater.*, 2019, **4**, 269–285.

4 T. Kim, W. Song, D. Son, L. Ono and Y. Qi, *J. Mater. Chem. A*, 2019, **7**, 2942–2964.

5 D. Chatterjee and A. Nandi, *J. Mater. Chem. A*, 2021, **9**, 15880–15918.

6 P. Simon and Y. Gogotsi, *Nat. Mater.*, 2008, **7**, 845–854.

7 Z. Zhai, L. Zhang, T. Du, B. Ren, Y. Xu, S. Wang, J. Miao and Z. Liu, *Mater. Des.*, 2022, **221**, 111017.

8 M. Mastragostino, C. Arbizzani and F. Soavi, *J. Power Sources*, 2001, **97**, 812–815.

9 L. Zhang, D. Shi, T. Liu, M. Jaroniec and J. Yu, *Mater. Today*, 2019, **25**, 35–65.

10 J. Goudar, S. Thrinethra, S. Chapi, M. Murugendrappa, M. Saeb and M. Salami-Kalajahi, *Mater. Adv.*, 2025, **6**, 2400271.

11 P. Kumari, S. Ghosh, V. Perla, C. Saha, H. Singh and K. Mallick, *J. Mater. Sci.: Mater. Electron.*, 2024, **35**, 1882.

12 P. Kumari, V. Perla, S. Ghosh, C. Saha, P. Kommu and K. Mallick, *J. Electron. Mater.*, 2024, **53**, 1498–1507.

13 J. Zhang, M. Gu and X. Chen, *Micro Nano Eng.*, 2023, **21**, 100229.

14 W. Chu, Z. Shi, Y. Hou, D. Ma, X. Bai, Y. Gao and N. Yang, *ACS Appl. Mater. Interfaces*, 2020, **12**, 2763–2772.

15 S. Chandrasekaran, L. Yao, L. Deng, C. Bowen, Y. Zhang, S. Chen, Z. Lin, F. Peng and P. Zhang, *Chem. Soc. Rev.*, 2019, **48**, 4178–4280.

16 C. Li, J. Balamurugan, D. C. Nguyen, N. H. Kim and J. H. Lee, *ACS Appl. Mater. Interfaces*, 2020, **12**, 21505–21514.

17 T. Wang, H. C. Chen, F. Yu, X. S. Zhao and H. Wang, *Energy Storage Mater.*, 2019, **16**, 545–573.

18 X. Long, Z. Wang, S. Xiao, Y. An and S. Yang, *Mater. Today*, 2016, **19**, 213–226.

19 B. Jiang, X. Ban, Q. Wang, K. Cheng, K. Zhu, K. Ye, G. Wang, D. Cao and J. Yan, *J. Mater. Chem. A*, 2019, **7**, 24374–24388.

20 I. Rabani, J. Yoo, H. Kim, D. Lam, S. Hussain, K. Karuppasamy and Y. Seo, *Nanoscale*, 2021, **13**, 355–370.

21 S. Ghosh, P. Kumari, C. Saha, H. Singh, I. Waziri, C. M. Morema and K. Mallick, *ChemistrySelect*, 2024, **9**, e202402255.

22 R. Bulakhe, S. Sahoo, T. Nguyen, C. Lokhande, C. Roh, Y. Lee and J. Shim, *RSC Adv.*, 2016, **6**, 14844–14851.

23 G. Li, Y. Feng, Y. Yang, X. Wu, X. Song and L. Tan, *Nano Mater. Sci.*, 2024, **6**, 174–192.

24 S. Ghosh, P. Kumari, H. Singh and K. Mallick, *J. Alloys Compd.*, 2024, **976**, 173178.

25 I. Melkiyur, Y. Rathinam, P. S. Kumar, A. Sankaiya, S. Pitchaiya, R. Ganesan and D. Velauthapillai, *Renewable Sustainable Energy Rev.*, 2023, **173**, 113106.

26 L. Zhang, D. Shi, T. Liu, M. Jaroniec and J. Yu, *Mater. Today*, 2019, **25**, 35–65.

27 S. Dhas, P. Maldar, M. Patil, A. Nagare, M. Waikar, R. Sonkawade and A. Moholkar, *Vacuum*, 2020, **181**, 109646.

28 B. Wiston and M. Ashok, *Mater. Lett.*, 2019, **235**, 76–79.

29 S. Charis Caroline, B. Das, S. Pramana and S. Batabyal, *J. Energy Storage*, 2023, **68**, 107812.

30 S. Liu, K. V. Sankar, A. Kundu, M. Ma, J. Kwon and S. Jun, *ACS Appl. Mater. Interfaces*, 2017, **9**, 21829–21838.

31 J. Yang, P. Xiong, C. Zheng, H. Qiu and M. Wei, *J. Mater. Chem. A*, 2014, **2**, 16640–16644.

32 M. Shao, R. Zhang, Z. Li, M. Wei, D. G. Evans and X. Duan, *Chem. Commun.*, 2015, **51**, 15880–15893.

33 F. Song, L. Bai, A. Moysiadou, S. Lee, C. Hu, L. Liardet and X. Hu, *J. Am. Chem. Soc.*, 2018, **140**, 7748–7759.

34 Z. Gao, J. Wang, Z. Li, W. Yang, B. Wang, M. Hou, Y. He, Q. Liu, T. Mann, P. Yang, M. Zhang and L. Liu, *Chem. Mater.*, 2011, **23**, 3509–3516.

35 C. Long, M. Zheng, Y. Xiao, B. Lei, H. Dong, H. Zhang, H. Hu and Y. Liu, *ACS Appl. Mater. Interfaces*, 2015, **7**, 24419–24429.

36 J. Liang, B. Tian, X. Zhang, C. Jiang, D. He and W. Wu, *J. Mater. Chem. A*, 2023, **11**, 3493–3503.

37 P. Kumari, C. Saha, S. K. Ghosh, V. K. Perla, H. Singh and K. Mallick, *New J. Chem.*, 2025, **49**, 234–245.

38 S. Ghazisaeed, M. Minuddin, H. Nakotte and B. Kiefer, *J. Appl. Crystallogr.*, 2020, **53**, 117–126.

39 K. Nakamoto, *Infrared and Raman Spectra of Inorganic and Coordination Compounds, Part B*, John Wiley & Sons, Inc., Hoboken, New Jersey, 2009 ISBN: 978-0-471-74493-1.

40 Y. Ke, Y. Li, L. Zhu, Y. Zhou and D. Liu, *SN Appl. Sci.*, 2020, **2**, 424.

41 J. Liang, B. Tian, X. Zhang, C. Jiang, D. He and W. Wu, *J. Mater. Chem. A*, 2023, **11**, 3493–3503.

42 S.-K. Geng, Y. Zheng, S.-Q. Li, H. Su, X. Zhao, J. Hu, H.-B. Shu, M. Jaroniec, P. Chen, Q.-H. Liu and S.-Z. Qiao, *Nat. Energy*, 2021, **6**, 904–912.

43 G. Kalaiyarasan, D. Lee, J. W. Lee and M. J. Ko, *ACS Appl. Mater. Interfaces*, 2024, **16**, 69142–69152.

44 Y. J. Yang, J. Dong, C. Zhang, X. Ding, Y. Li, H. Ren and F. Guo, *J. Electroanal. Chem.*, 2021, **895**, 115537.

45 A. Gayathri, S. Mathi, M. Vijayarangan, J. Jayabharathi and V. Thanikachalam, *ChemistrySelect*, 2022, **7**, 45.

46 G. Kuntoji, N. Kousar, S. Gaddimath and L. K. Sannegowda, *Biosensors*, 2024, **14**, 277.

47 Y. Qiu, Y. Lin, H. Yang and L. Wang, *J. Alloys Compd.*, 2019, **806**, 1315–1322.

48 Y. J. Yang, Y. Li, X. Ding, C. Zhang, H. Ren, F. Guo and J. Dong, *J. Alloys Compd.*, 2021, **871**, 159510.

49 Y. J. Yang, M. Liu, C. Jiang, P. Yang, N. Wang, S. Chen and Y. Cheng, *J. Energy Storage*, 2021, **44**, 103462.

50 Y. J. Yang, J. Dong, C. Zhang, X. Ding, Y. Li, H. Ren and F. Guo, *J. Electroanal. Chem.*, 2021, **895**, 115537.

51 J. Zhuge, F. Rouhani, F. Bigdeli, X. Gao, H. Kaviani, H. Li, W. Wang, M. Hu, K. Liu and A. Morsali, *Dalton Trans.*, 2021, **50**, 2606–2615.

52 S. Sarr, N. F. Sylla, D. T. Bakhoum, K. O. Oyedotun, B. D. Ngom and N. Manyala, *J. Energy Storage*, 2021, **43**, 103294.

53 J. J. William, S. Balakrishnan, M. Murugesan, M. Gopalan, A. J. Britten and M. Mkandawire, *Mater. Adv.*, 2022, **3**, 8288–8297.

54 J. J. William, I. M. Babu and G. Muralidharan, *New J. Chem.*, 2019, **43**, 15375–15388.

55 J. J. Benitto, J. J. Vijaya, B. Saravanakumar, H. Al-Lohedan and S. Bellucci, *RSC Adv.*, 2024, **14**, 8178–8187.

56 E. G. C. Neiva and A. J. G. Zarbin, *New J. Chem.*, 2022, **46**, 11118–11127.

57 X. Zhang, J. Jiang, Y. Chen, K. Cheng, F. Yang, J. Yan, K. Zhu, K. Ye, G. Wang, L. Zhou and D. Cao, *Chem. Eng. J.*, 2018, **335**, 321–329.

58 K. Subramani, N. Sudhan, R. Divya and M. Sathish, *RSC Adv.*, 2017, **7**, 6648–6659.

59 Z. Song, W. Liu, Q. Zhou, L. Zhang, Z. Zhang, H. Liu, J. Du, J. Chen, G. Liu and Z. Zhao, *J. Power Sources*, 2020, **465**, 228266.

60 P. Matheswaran, P. Karuppiah, S. M. Chen, P. Thangavelu and B. Ganapathi, *ACS Omega*, 2018, **3**, 18694–18704.

61 G. Rutavi, D. J. Tarimo, V. M. Maphiri and N. Manyala, *Int. J. Energy Res.*, 2022, **46**, 11214–11227.

62 M. N. Rantho, M. J. Madito, F. O. Ochai-Ejeh and N. Manyala, *Electrochim. Acta*, 2018, **260**, 11–23.